ingegneria sismica
International Journal of Earthquake Engineering
Anno XLIII - Num. 1 - 2026

Research on the coordinated balancing strategy of renewable energy system power and electricity based on spatio-temporal resource prediction

Qiang Xiao[1], *Mi Zhang*[1], *Jingbo Ma*[1], *Jian Zhang*[2,*] *and Yuguo Chen*[2]

[1] New-Type Power System Construction Center, State Grid Chongqing Economic and Technology Research Institute, Chongqing, 401121, China
[2] Beijing Tsintergy Technology Co., Ltd., Beijing, 100080, China

SUMMARY: *As the proportion of renewable energy power generation and the proportion of participation in market transactions continue to expand, the stochastic and volatile nature of renewable energy power generation makes it difficult for the current power coordination and balancing method to be applied to a high proportion of renewable energy power systems. This paper proposes a coordinated power balancing strategy for renewable energy systems based on spatio-temporal resource prediction, using ARIMA-LSTM model to predict renewable energy system loads and scenery resources, constructing a coordinated power balancing model, and solving it by using mixed integer programming method. The results show that the proposed ARIMA-LSTM model is not only compatible with the prediction of multivariate loads such as cold, heat, gas, electricity, etc., but also can be used for the prediction of wind speed, radiant illuminance, etc., and the MAPE error values in the prediction time period of one week are 6.05%, 1.88%, and 9.50%, which are lower than that of the models of ARIMA, LSTM, and Elman, and have better adaptability and prediction accuracy. The proposed stochastic power coordinated balancing model and algorithm are verified to be correct and effective by simulating and analyzing a high hydropower proportion system as an example.*

KEYWORDS: *spatio-temporal resource prediction; ARIMA-LSTM; renewable energy; coordinated power balancing; mixed integer programming.*

1 Introduction

The energy shortage and ecological damage have caused the clean, low-carbon, safe and efficient concept to be the leading trend of energy development in the contemporary world over the last few years. It is thus necessary to increase the share of clean energy sources and expand the use of renewable energy production and consumption as part of developing such an energy system [1, 2]. With this aim, various countries have hastened the implementation of hydropower, wind power, photovoltaic generation, and other renewable resources, and power systems with high renewable share will become crucial future trend. Nevertheless, as this transition continues to develop, the primary challenges confronting the renewable industry shift to system flexibility constraints, regulatory capacity, and electricity market mechanisms [3, 4]. Large-scale integration of these resources into the power grid presents operational and dispatch risks due to the nature of wind and solar output, which is inherently unpredictable and intermittent, and the forecast accuracy varies significantly depending on the time horizon. In

*zhangjujs126@.com
https://doi.org/10.65102/is2026453
Published: 30 April, 2026

turn, renewable generation is frequently limited, and the curtailing of wind, solar, and hydroelectricity is very extreme, wasting a lot of energy and compromising environmental performance as well as economic performance [5-9]. Nevertheless, the fact that renewable generation has generated more environmental advantages does not diminish the significance of preserving power and energy balance, as peaking costs and other financial issues rise [10, 11].

Spatio-temporal prediction models use data analysis and modeling techniques to predict future changes in time and space. It is based on past observational data and known correlations to predict future time and place through methods such as statistical modeling, machine learning or deep learning, and is used in a variety of fields, including meteorology, transportation planning, urban development and natural disaster management. Kath et al. explore the profitability of power trading using renewable energy forecasts by energy trading firms, where forecasting models improved by regression models significantly boost profits, and designing contracts that include risk-sharing is a key performance driver for balancing risk and return for both parties [12]. In comparison with traditional prediction methods, spatio-temporal prediction models are more efficient in deriving dynamic spatial and temporal features, improving the accuracy of renewable power prediction and promoting improved economic performance. Yang et al proposed a hybrid sequence prediction model using time-space attention to improve power prediction in changing wind conditions. Depending on the level of variation of wind speeds, the model can switch automatically and switch to a wind turbine characteristic curve model in case of large variations, where the prediction error is reduced [13]. Zhang et al. created a feature matrix on a weighted correlation coefficient, combined convolutional neural networks (CNNs) and long short-term memory (LSTM) networks to learn sequential dependencies, and proposed a novel method using spatio-temporal correlation that significantly improves the accuracy of wind-farm cluster output predictions[14]. Su et al. introduced an innovative PV forecasting model, which includes the combination of graph neural networks and Fourier transforms; it also uses the joint representation of spatio-temporal dependencies with hypervariable maps and identification of critical periodic patterns with frequency domain data, which is much more powerful in terms of accuracy and generalization of multi-site PV prediction [15]. Admasie et al. used a hyper-parameter optimized LSTM model to predict the day-ahead generation of renewable energy sources and used the Gray Wolf optimization algorithm for generation scheduling, which effectively reduces the system operating cost and mitigates power fluctuations [16]. The authors Su et al. produced graph-structured data based on gray relational analysis and added an attention-based spatio-temporal graph CNN to obtain dynamic relationships between load variables and meteorological parameters, which significantly improved the precision of short-term load prediction of regional integrated energy systems [17]. Ge et al. proposed a novel framework to forecast the short term output of regional hydro-wind-photovoltaic clusters, to overcome the stochastic randomness and the heterogeneity of renewable generation. Their approach led to a significant improvement in the performance of their forecasting method by quantifying the correlation between meteorology and power via different spatio-temporal hybrid networks and spatio-temporal lag-correlation analysis[18].

This paper presents the development of a spatio-temporal resource forecasting model based on ARIMA-LSTM to ensure an orderly balancing of power output among various units of the power system. Moreover, a power coordination and balance model of a multi-source hybrid energy system is implemented, which considers renewable sources, including wind, solar, cascade hydropower, and thermal generation. The solution is obtained through the mixed-integer linear programming process, which leads to a coordination and balancing plan of renewable-dominated energy systems. To test the suggested method, the experimental comparison between ARIMA-LSTM and ARIMA, LSTM, Elman, and other benchmark algorithms is conducted, and the system with a fairly high percentage of hydropower is chosen

to perform the analysis of the numerical applications.

2 Energy system resource prediction based on ARIMA-LSTM modeling

In this chapter, the time series forecasting model ARIMA-LSTM is constructed to realize the forecasting of renewable energy system loads and scenery resources.

2.1 Spatio-temporal resource prediction model based on ARIMA-LSTM

The load series of renewable energy systems has linear and nonlinear features, and there is no one single prediction method, which would be capable of reflecting all its dynamics. This study will overcome this challenge by integrating linear and nonlinear models to predict the load on the system as well as wind and solar power sources. Linear ARIMA model is initially used to approximate the load demand, wind speed, solar irradiance time series and other relevant variables such that linear elements in the data can be eliminated as far as possible. The residual sequence not yet explained is afterwards modeled by the nonlinear LSTM model, which is used to predict the fitting error and subsequently refine the final result. This allows using the benefits of the linear and nonlinear methods simultaneously to reach enhanced performance of overall forecasting.

2.1.1 Linear ARIMA models

The ability and flexibility of the ARIMA model in time series analysis has been widely demonstrated. The $ARIMA(p,d,q)$ model consists of a p-order autoregressive model, $AR(p)$, a q-order moving average model, $MA(q)$, and a number of difference times d to generate the smoothed series. Nonstationary time-series data are transformed into smoothed sequences during the differencing operation after which regression is done on the lagged values of the dependent variable as well as the current and lagged terms of the random error. The optimal order used in this case is based on the Akaike Information Criterion (AIC) and the final $ARIMA(4,1,20)$ model is determined accordingly. This formulation meets the stationarity condition and it is very efficient at reducing the stochastic fluctuations that affect the forecasting accuracy.

2.1.2 Nonlinear LSTM modeling

Neural networks are effective methods of estimating non-linear functions and have been widely used on nonlinear analysis problems. Of these, recurrent neural networks (RNNs) are popularly used in processing and predicting sequential data and are typically trained using backpropagation through time or real-time recurrent learning algorithms. Nevertheless, during long sequences, optimization usually encounters the problem of vanishing or exploding gradients that can cause unsatisfactory training results. To address this, a Long Short-Term Memory (LSTM) network was created as a modification of RNN. It has been expressly constructed to reduce the vanishing gradients and maintain valuable data over a long time scale. The LSTM network consists of an input layer, and output layer and a number of hidden layers in between. The hidden layers are arranged in memory units, with every unit possessing three gating mechanisms, namely, forget gate, input gate, and output gate. The typical memory cell design of the LSTM network is shown in Fig. 1.

In the forgetting gate, each input x_t, the previous moment cell output h_{t-1} and the

previous moment cell state c_{t-1} together determine the forgotten part of the state memory cell. In the input gate, the cell state c_{t-1} is updated to c_t under the activation of the sigmoid and tanh functions. In the output gate, the updated unit state c_t is once again passed through the sigmoid and tanh functions, selectively outputting h_t .The LSTM neural network unit can be defined by the following set of equations:

$$f_t = \sigma\left(W_f\left[h_{t-1}, x_t\right] + b_f\right) \tag{1}$$

$$i_t = \sigma\left(W_i\left[h_{t-1}, x_t\right] + b_i\right) \tag{2}$$

$$o_t = \sigma\left(W_o\left[h_{t-1}, x_t\right] + b_o\right) \tag{3}$$

$$g_t = \tanh\left(W_g\left[h_{t-1}, x_t\right] + b_g\right) \tag{4}$$

$$c_t = g_t \cdot i_t + f_t \cdot c_{t-1} \tag{5}$$

$$h_t = o_t \cdot \tanh\left(c_t\right) \tag{6}$$

where f_t, i_t, o_t, g_t denote the forgetting gate, input gate, output gate, alternative states, respectively. c_t, h_t denote the current input updated cell state, current prediction or output state, respectively. W_f, W_i, W_o, W_g denote the weight matrices of the corresponding gates, respectively. b_f, b_i, b_o, b_g denote the offset of each corresponding gate, respectively. σ denotes the sigmoid activation function. $\tanh$ denotes the hyperbolic tangent activation function. $\cdot$ denotes the elementwise multiplication of elements in a vector.

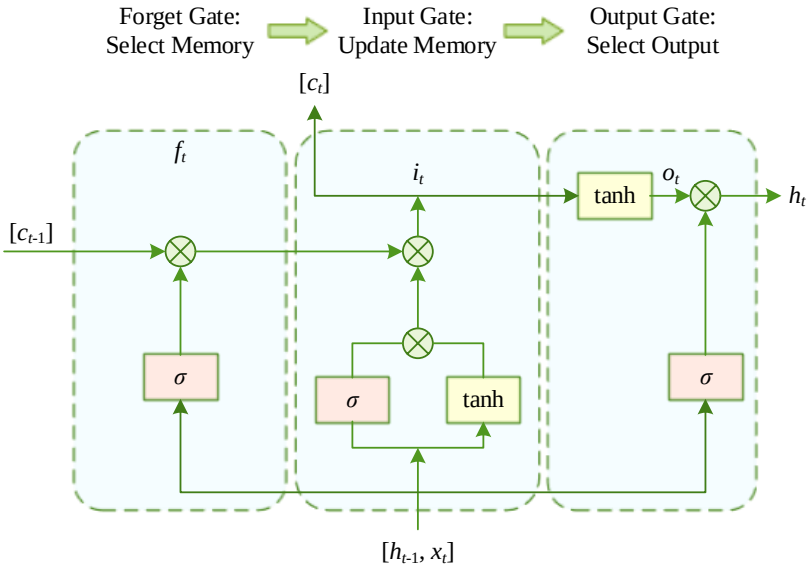

Figure 1: Standard LSTM network memory unit

2.1.3 Combined ARIMA-LSTM models

Let the original load dataset be $H=\left[h_1,h_2,h_3,\cdots,h_n\right]$, and use the ARIMA model to obtain the fitted sequence of historical data for H, $A=\left[A_1,A_2,A_3,\cdots,A_n\right]$ and the forecast sequence $P_t=\left[P_1,P_2,P_3,\cdots,P_t\right]$. Comparing the fitted values with the actual values of the load, the fitted error sequence $\Delta A=\left[\Delta A_1,\Delta A_2,\Delta A_3,\cdots,\Delta A_n\right]$ is obtained and is calculated by the formula:

$$\Delta A_i=h_i-A_i,\ i=1,2,3,\cdots,n \tag{7}$$

The fitted error sequence ΔA reduces the influence of linear components to some extent, which makes the nonlinear characteristics of the load stronger. Since the neural network model has a high capability to learn nonlinear patterns it is appropriate to use this model to correct the fitted error sequence. In turn, the presented paper uses an LNN neural network to approximate the residual error series ΔA and hence derive the nonlinear error prediction term ΔL_t, which can be expressed as follows:

$$\Delta L_t=f\left(\Delta A_{t-1},\Delta A_{t-2},\cdots,\Delta A_{t-n}\right)+\varepsilon_t \tag{8}$$

where: $f\left(\cdot\right)$ denotes nonlinear modeling of LSTM. The ε_t denotes random error, which cannot be predicted.

The predicted value ΔL_t is used as the loading error prediction result, further learning the nonlinear characteristics of the error sequence, outputting a stable and valid prediction result and error correction, and finally obtaining the prediction result of the combined ARIMA-LSTM model as:

$$P_{At}=P_t+\Delta L_t \tag{9}$$

The prediction steps of the combined ARIMA-LSTM model proposed in this paper are:

(1) Input the similar day load training set data into the ARIMA model to get the linear load prediction value.

(2) Compare the load training data and linear fitting data to obtain the fitting error series.

(3) Combine the key factor data of similar days and predict the fitting error sequence using LSTM model.

(4) Add the linear fit predictions with the nonlinear error predictions to obtain the final load prediction results of the combined model.

2.2 Modeling Examples

2.2.1 Case Overview and Determination of Data Training Set

The chapter uses 8760 hours of multivariate data gathered in 2023 on airport energy island and some of the datasets are resources of heating, cooling, electricity, gas demand, wind speed, solar irradiance and other variables. Out of these, the 744 hours recorded in January are chosen as sample data, and a hybrid framework is used to predict load conditions in February. The reliability of models is subsequently tested by comparing them to the reference data. To find the most appropriate model in case of ARIMA, the first half of the sample set is considered as a training subset and the other half as a testing subset. Once the ARIMA structure has been

defined and applied to the sample series, the resultant residual sequence is split into two halves and the first half is trained and the second half is tested in order to get the best LSTM network.

2.2.2 Forecasting process

Using heat-load prediction as an illustrative example, the process can be defined as below:

(1) Smoothness test to check the smoothness of the data. Heat, cooling and electricity data are stationary as the samples mean and variance of these data converge roughly to constant levels over time and can be modeled. On the other hand, the wind-speed data are nonstationary and are stabilized upon first-order differencing.

(2) The model order is subsequently established. Calculating the smallest AIC value is done with Python. The findings indicate that the AIC attains its lowest at$p$=4, d=1, q=20, so the time series model is determined as $ARIMA(4,1,20)$.

(3) Thereafter, the ARIMA formulation is used to directly predict the energy-island load between February 1 and February 7, providing the linear prediction sequence of the February heat load that is subsequently compared to the real measurements.

(4) Once the ARIMA structure has been identified, the fitted residual series can be obtained. The first half of this residual sequence is used to train, and last half is used as a test set to choose the best LSTM network.

In repeated experiments, the initial learning rate that is used in training the LSTM model is 0.001, but after training 130 epochs, the learning rate is reduced, and the network performs optimally at a decay factor of 0.3. The trained model is used to predict the load in February, and the nonlinear predicted load in February is obtained ΔL_t.

(5) Equation (9) is used to obtain the ARIMA-LSTM model integrated forecast sequence P_{At}. At this point, the integrated prediction of heat load is completed, and the same method is used to obtain the electric load, wind speed prediction sequence, and the cold load is zero.

2.2.3 Analysis of forecast results

In order to compare the predictive power of various methods, the ARIMA model, LSTM model, Elman model, ARIMA-LSTM hybrid framework are used to predict the heat load, electrical load and wind speeds of the energy island every hour between Feb 1-7. The daily average absolute percentage error (MAPE) is subsequently determined. The error curves that relate to the forecasting outcomes of each approach are given in Fig. 2, with (a)-(c) being used to denote the results of the heat load, electric load and wind speed respectively.

The findings indicate that electrical load forecasting has the greatest similarity to measurements and the two series are relatively stable. Heat-load prediction comes next, whereas wind-speed prediction is the worst one and has a lower fit as compared to the first two indicators. However, all of the three predicted sequences exhibit the same general trend as the observed data and the deviation is kept at a reasonable level. This indicates that the ARIMA-LSTM hybrid structure used in this paper is effective in providing forecasting results on the loads of renewable-resource systems along with variables of wind and solar resources.

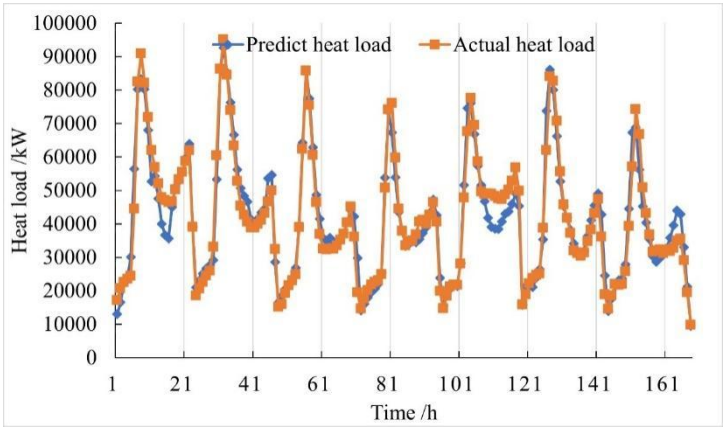

(a) Heat load forecasting

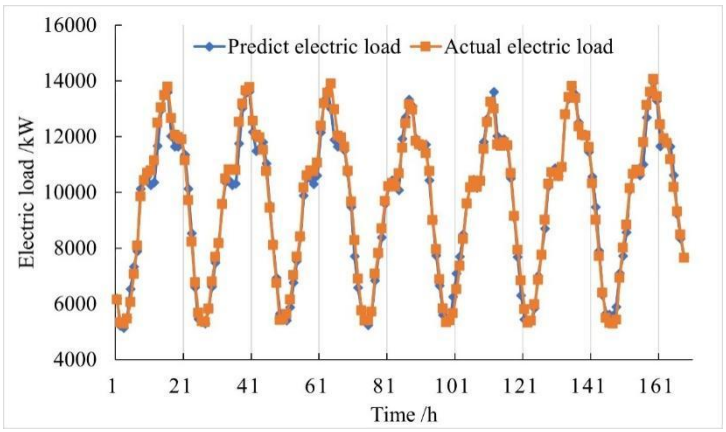

(b) Electric load forecasting

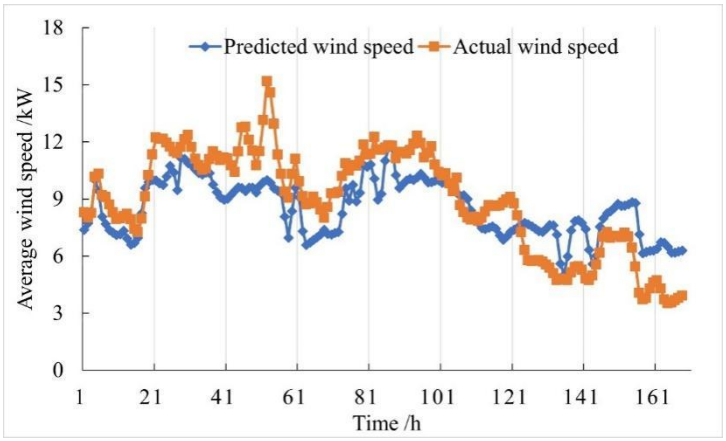

(c) Wind speed prediction

Figure 2: Comparison between the comprehensive prediction results and the actual situation

The comparison of prediction errors of heat load, electric load and wind speed from February 1 to 7 for each model is shown in Tables 1 to 3, respectively. It can be seen that the prediction effect of electric load is relatively more satisfactory, and the relative average error MAPE of the four models is within 4%. The errors of heat load and wind speed are relatively larger due to their own characteristics, but they are basically controlled within a certain range.

Meanwhile, compared with the other three models, the ARIMA-LSTM hybrid model in this paper has the smallest MAPE in the prediction of heat load, electric load, and wind speed, which are 6.05%, 1.88%, and 9.50%, respectively, with the best prediction effect, and the prediction effect of the ARIMA model is the most unsatisfactory among these methods.

Table 1: Comparison of heat load forecasting error

Time	Model prediction error /%			
	ARIMA	LSTM	Elman	ARIMA-LSTM
February 1st	16.07	16.07	15.67	13.75
February 2nd	11.92	10.31	8.99	6.47
February 3rd	5.96	5.66	8.08	4.44
February 4th	8.18	6.06	7.48	6.06
February 5th	12.23	8.59	11.12	4.24
February 6th	8.18	7.78	8.99	5.96
February 7th	11.83	11.22	13.24	7.48
Mean	9.30	8.21	9.20	6.05

Table 2: Comparison of electric load forecasting error

Time	Model prediction error /%			
	ARIMA	LSTM	Elman	ARIMA-LSTM
February 1st	4.85	3.55	3.85	2.34
February 2nd	4.63	3.25	3.25	2.99
February 3rd	4.11	2.90	2.47	1.52
February 4th	4.55	2.81	2.90	1.69
February 5th	4.11	3.72	4.16	2.68
February 6th	3.60	3.03	3.72	2.34
February 7th	3.85	2.81	2.95	1.47
Mean	3.71	2.76	2.91	1.88

Table 3: Comparison of wind speed forecasting error

Time	Model prediction error /%			
	ARIMA	LSTM	Elman	ARIMA-LSTM
February 1st	8.55	9.59	7.97	5.89
February 2nd	10.2	3.69	8.43	4.84
February 3rd	19.64	15.25	13.87	12.94
February 4th	10.63	11.78	12.82	8.43
February 5th	11.78	10.28	9.93	7.04
February 6th	26.35	20.45	27.62	24.15
February 7th	19.41	16.29	15.13	12.71
Mean	13.32	10.92	11.97	9.50

In order to compare the effect of the training set on the prediction results, taking one kind of load as an example, the errors of the prediction results obtained with the training set of one week, one month and one year were tested as shown in Table 4.

The analysis shows that LSTM model, as a more popular model nowadays, has received great attention for its high prediction accuracy and the fact that only historical data are needed for prediction. The ARIMA-LSTM combined model established in this paper not only has better prediction accuracy compared with the LSTM model, but also ensures that there is little difference in the length of the operation, and the model will be more reliable when the training set is smaller.

Table 4: The heat load prediction errors corresponding to different models

Model	Training set length /h	The duration of calculation /min	MAPE /%
ARIMA	168	1.14	9.30
ARIMA	720	3.43	10.27
ARIMA	8760	11.36	9.15
LSTM	168	5.72	8.21
LSTM	720	18.21	6.48
LSTM	8760	125.37	5.05
ARIMA-LSTM	168	6.85	6.05
ARIMA-LSTM	720	20.52	4.86
ARIMA-LSTM	8760	137.87	3.47

3 Renewable energy system electric power coordination and balancing strategy research

On the basis of the forecast of renewable energy system load and wind and solar resources, this chapter proposes the coordinated balancing strategy of electric power, i.e., constructing the coordinated balancing model of electric power for renewable energy system and solving it by linear programming method to realize the optimal dispatch and coordinated balancing of electric power for electric power system.

3.1 Coordinated Balance of Power Models for Renewable Energy Systems

3.1.1 Objective function

The objective function of the multi-objective optimization model of coordinated balance of electricity power of renewable energy system based on spatio-temporal resource prediction consists of 2 parts: the 1st part is the minimum of the sum of the deviation of the power completion of each transaction, which guarantees the successful completion of each transaction, and introduces the priority level factor and the weight coefficient to determine the decomposition order of the transactions of different priority levels. The 2nd part is to minimize the deviation between renewable energy power generation and theoretical power, which ensures the maximization of renewable energy consumption. The specific expression of the objective function is:

$$\min\left\{\sum_{r=1}^{N_r}\left(\eta_r\sum_{\theta=1}^{\Theta}\gamma_{r,\theta}\varepsilon_{n,r,\theta}^{NE}\right)+\eta_{r+1}\varepsilon_{r+1}^{NE}\right\} \tag{10}$$

where: N_r is the total number of priority levels for medium and long term trading. r is the priority rank number, the smaller the value of r, the higher the priority rank. η_r is the priority level factor, which specifies $\eta_r \gg \eta_{r+1}$ to ensure that secondary objectives are considered on the basis of the realization of the objectives of the r th level. Θ is the total number of transaction types under the same priority level. θ is the serial number of different transactions under the same priority. $\gamma_{r,\theta}$ is the weight coefficient of each transaction under the same priority level. Generally, it is recommended that the weight coefficients under the same priority level should be selected according to the principle of $\sum_{\theta=1}^{\Theta}\gamma_{r,\theta}=1$, and the larger the value of

$\gamma_{r,\theta}$, the higher the degree of importance. $\varepsilon_{n,r,\theta}^{NE}$ is the deviation from completion of the θ type of trading contract at the r th level for renewable energy sources in region n, positive. ε_{r+1}^{NE} is the amount of deviation, positive, between renewable energy generation and theoretical renewable energy power.

3.1.2 Constraints

(1) Load balancing constraints:

$$P_n^{NE}(t)+\sum_{g=1}^{N_{G,n}}P_{g,n}(t)+\sum_{m=1}^{N}L_{n,m}(t)=P_n^{L}(t)+L_n^{out}(t) \tag{11}$$

where: n and m are the grid partition numbers, N is the number of grid partitions, g is the serial number of thermal power units, $N_{G,n}$ is the total number of thermal power units in the region n, $P_n^{NE}(t)$ is the renewable energy output in the region n at the moment t, $P_{g,n}(t)$ is the power output of the g thermal unit in the region n at t moment, $P_n^{L}(t)$ is the load in the region n, $L_{n,m}(t)$ is the power exchange between the region n and the region m at t moment, and $L_n^{out}(t)$ is the outgoing power from the contact line in the region n at t moment.

(2) Conventional unit/heating unit output constraints:

$$0\le\Delta P_{g,n}(t)\le\left(P_{g,n}^{\max}(t)-P_{g,n}^{\min}(t)\right)X_{g,n}(t) \tag{12}$$

$$P_{g,n}(t)=P_{g,n}^{\min}(t)X_{g,n}(t)+\Delta P_{g,n}(t) \tag{13}$$

where: $P_{g,n}^{\max}(t)$ and $P_{g,n}^{\min}(t)$ are the upper and lower limits of the output of the g th thermal power unit in the region n at the moment t, respectively. $X_{g,n}(t)$ is the operating state of the g thermal power unit in the region n at the moment t, it is a binary variable, the value of 0 means the unit has been shut down, and the value of 1 means the unit is running. The $\Delta P_{g,n}(t)$ is the power of the g thermal unit in region n that participates in the optimization at moment t.

(3) Conventional unit/heating unit ramp-up constraint:

$$P_{g,n}(t+1)-P_{g,n}(t)\le\Delta P_{g,up} \tag{14}$$

$$P_{g,n}(t)-P_{g,n}(t+1)\le\Delta P_{g,down} \tag{15}$$

where: $\Delta P_{g,up}$ and $\Delta P_{g,down}$ are the upward and downward creep rates of the g th thermal power unit at the t th moment, respectively.

(4) Logical constraints on the starting and stopping operation status of the unit:

$$\begin{cases} X_g(t) - X_g(t-1) - Y_g(t) + Z_g(t) = 0 \\ -X_g(t) - X_g(t-1) + Y_g(t) \le 0 \\ X_g(t) + X_g(t-1) + Y_g(t) \le 2 \\ -X_g(t) - X_g(t-1) + Z_g(t) \le 0 \\ X_g(t) + X_g(t-1) + Z_g(t) \le 2 \end{cases} \tag{16}$$

where: $X_g(t)$ is the operating state of the g th thermal power unit at the moment t. $Y_g(t)$ and $Z_g(t)$ are the startup state and shutdown state of the g th thermal power unit at the moment of t, respectively, which are binary variables.

For $Y_g(t)$, a value of 0 indicates that it is not in the startup state, and a value of 1 indicates that it is starting up. For $Z_g(t)$, a value of 0 indicates that it is not in the shutdown state, and a value of 1 indicates that it is shutting down. Eq. (16) is a logical constraint on the start-stop and operating states of the unit, which ensures that the state variables are logical in the process of unit combination.

(5) Minimum startup and shutdown time constraints for conventional thermal/heating units:

$$Y_g(t) + Z_g(t+1) + Z_g(t+2) + \cdots + Z_g(t+k) \le 1 \tag{17}$$

$$Z_g(t) + Y_g(t+1) + Y_g(t+2) + \cdots + Y_g(t+k) \le 1 \tag{18}$$

where the parameter k is determined by the minimum startup or shutdown time parameter of the unit, which reflects the minimum startup or shutdown time step, this constraint is mainly considered to be constrained by the physical characteristics of the unit, the energy consumption of the unit, and the operating cost, and the unit can not be started and stopped frequently.

(6) Grid line transmission capacity constraint:

$$\left|L_{n,m}(t)\right| \le L_{n,m}^{\max}(t) \tag{19}$$

where: $L_{n,m}^{\max}$ is the line transmission section limit.

(7) System spare capacity constraint:

$$\sum_{n=1}^{N}\sum_{g=1}^{N_{G,n}} P_{g,n}^{\max}(t) X_{g,n}(t) + \sum_{n=1}^{N} R_n^{NE} \ge \sum_{n=1}^{N}\left(P_n^L(t) + L_n^{out}(t)\right) + R_P \tag{20}$$

$$\sum_{n=1}^{N}\sum_{g=1}^{N_{G,n}} P_{g,n}^{\min}(t) X_{g,n}(t) \le \sum_{n=1}^{N}\left(P_n^L(t) + L_n^{out}(t)\right) + R_N \tag{21}$$

where: R_P and R_N are the positive spinning reserve and negative spinning reserve, respectively. R_n^{NE} is the credible capacity of renewable energy generation in region n, which refers to the capacity of conventional units that can be replaced by renewable energy under a certain confidence level.

Equation (19) ~ (21) for the system security operation constraints, to ensure that the monthly trading power in the daily scheduling level of enforceability.

(8) Renewable energy trading power constraints:

$$\sum_{t=1}^{T} p_{n,r,\theta}^{NE}(t) + \varepsilon_{n,r,\theta}^{NE} = Q_{n,r,\theta}^{NE} \tag{22}$$

where: $p_{n,r,\theta}^{NE}(t)$ is the electricity of the θ type of trading contract at the r level for the renewable energy field stations in the region n at the moment t. T is the total time period. $Q_{n,r,\theta}^{NE}$ is the sum of the electricity of all renewable energy field stations in region n that sign the θ th trading contract under the r th level.

This constraint ensures that the sum of wind/PV power generation and deviation power in all optimization periods is equal to the minimum power generation required for trading power. At the same time, the deviation amount can turn the renewable energy trading power constraint into a soft constraint in the optimization model, thus avoiding the situation that the constraint is infeasible when the guaranteed power cannot be reached due to the peaking or sectional power restriction.

(9) Renewable energy generation output component constraint:

$$P_n^{NE}(t) = \sum_{r=1}^{N_r} P_{n,r}^{NE}(t) + P_{n,r+1}^{NE}(t) \tag{23}$$

$$0 \le \sum_{t=1}^{T} P_n^{NE}(t) + \varepsilon_{r+1}^{NE} \le \sum_{t=1}^{T} P_n^{NE*}(t) \tag{24}$$

where: $P_{n,r+1}^{NE}(t)$ is the surplus renewable energy output of region n at the $r+1$ th level at time t. $P_{n,r+1}^{NE}(t) \ge 0$ means that there is still room for acceptance in the grid after all the transactions have been completed by the renewable energy farms, and the renewable energy farms can continue to generate electricity. $P_n^{NE*}(t)$ is the theoretical power of renewable energy in region n at moment t.

3.2 Model Solution Methods

Monthly power decomposition formulation is a single-objective linear programming problem and may thus be directly solved with the Cplex solver. Conversely, the optimal formulations of weekly and day-ahead scheduling include nonlinear elements such as the thermal power fuel-cost function and the hydropower output function. Such nonlinear expressions in both objective and constraints need to be linearized to obtain modified versions of the original formulations, which are now mixed integer linear program models, more tractable to Cplex. Moreover, it also includes a multi-objective optimization problem.

3.2.1 Model linearization

The output characteristic of hydropower unit is a cluster of curves with nonlinear relationship with reservoir capacity and generation flow, indicating the relationship between the output of hydropower unit P_h and generation flow Q_h under different reservoir capacity V_s. Because changes in the volume of the reservoir and the hydraulic head cause different limits on generation and discharges, the output-characteristic curve of the hydropower unit needs to be linearized. In the same manner, the quadratic cost of thermal power unit fuel should also be transformed into a linear form and the method of treatment of each part is basically the same.

3.2.2 Multi-objective solving

The objective functions are typically conflicting in multi-objective optimization problems, and therefore feasible solutions that reach the optimum of all the objectives at the same time are not often present. Two common treatments are used in practice. The first one transforms the given multi-objective formulation into an equivalent one with a single-objective formulation, and the second one cuts it up into multiple scalar optimization problems. This work introduces the min-max normalization approach in order to reformulate the multi-objective formulation as a single-objective problem:

$$F = \min \sum_{i=1}^{3} w_i f_i' \tag{25}$$

$$f_i' = \frac{f_i^{\max} - f_i}{f_i^{\max} - f_i^{\min}} \tag{26}$$

where: w_i is the weight of the objective function, which can be set according to the actual operation requirements. f_i, f_i' are the values of the objective function before and after normalization, respectively. $f_i^{\min}$, $f_i^{\max}$ are the minimum and maximum values of the ith objective function, which are calculated as follows: single-objective optimization computation with f_1, f_2 and f_3 as the optimization objectives, and then extracting the corresponding extrema of the three solutions.

3.3 Example analysis

3.3.1 Algorithmic system

To evaluate the reasonableness and usability of the coordinated power-and-energy balancing model developed to implement the renewable energy system, one chooses to consider a regional system, where the share of hydropower is high as the study case. The peak load of the system is 900 MW. The installed capacities are 565 MW in thermal generation, 520 MW in hydropower, 160 MW in wind farm installations, and 110 MW in photovoltaic generation.

In order to examine the effect of a hydropower-based architecture and wind generation uncertainty on coordinated balancing, three cases have been developed to be used as a comparison:

Example 1: The power-balance analysis is done with no regards to uncertainty in wind and solar generation.

Example 2: Based on example 1, the wind generation uncertainty is additionally considered.

Example 3: In the context of example 2, the predictive error band of wind power production becomes larger.

3.3.2 Results of the algorithmic analysis

Figure 3 shows the power balance results of Case 1 with panels (a) and (b) being the result of hydropower and thermal generation respectively. Water spillage or renewable curtailment does not occur in this case because the system has a large amount of adjustable hydropower capacity but wind and photovoltaic generation installed capacities are relatively small. The discharge of run-of-river hydropower stations is constant and cannot be regulated arbitrarily, thus Fig. 3(a) only displays the dispatch results of the three adjustable hydropower stations. Hydropower

stations 1 and 2 are part of a cascade, with station 1 being located upstream.

According to Fig. 3(a) there is enough incoming water. Since hydropower station 2 is located at the bottom of the cascade, it works at or close to full capacity in most parts of a typical week in order to optimize clean-energy consumption and reduce water waste. Conversely, the flow into the HPPs 1 and 3 is lower than the maximum discharge that can be generated by them. In order to take advantage of the peak-shaving property of hydropower, the outputs of HPPs 1 and 3 differ significantly in various time intervals.

It can be seen in Figure 3(b) that thermal unit 1, with the highest capacity and lowest generation cost, stays in operation all through the normal week. This unit is run at full output during the weekday peak demand to have more economical performance. Its output is decreased when the weekend load decreases to meet the system peak-regulation needs. The commitment of thermal units 2 and 3 are based on the load level, and it is usually the case that only one of these two is necessary to meet the demand. It is important to note that on Tuesday a special scenario occurs since the load is at its highest of the week and wind production is also not very high, so all thermal units need to be activated to ensure the balance in the system.

Comparing Fig. 3(a) with Fig. 3(b), it is also evident that thermal generation varies fairly smoothly, but hydropower generation is much more variable, which suggests that hydropower performs the largest share of system peak-regulation work.

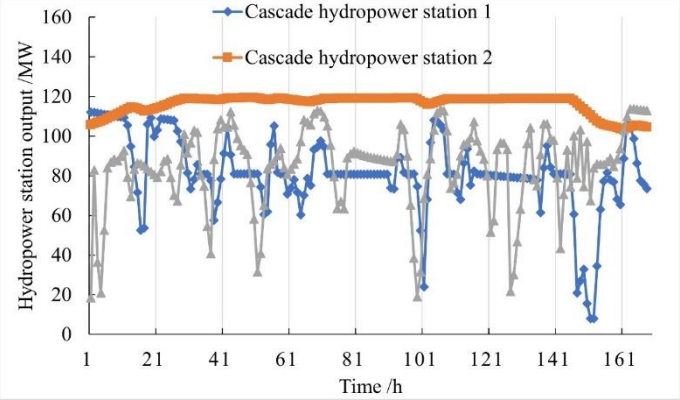

(a) Hydropower station

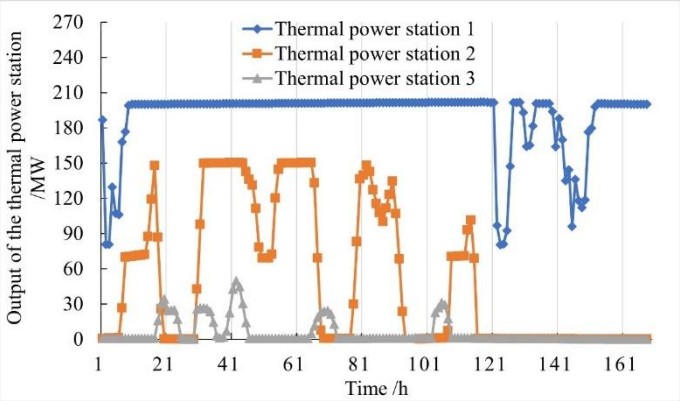

(b) Thermal power station

Figure 3: Typical output curves of hydropower stations and thermal power stations

The contribution of different power sources in the typical week power contribution and the proportion of contribution are shown in Table 5. It can be seen that the total power demand of

the load in a typical week is 112,593.26 MW-h, of which four hydropower plants contribute 51.74% to the system power, which is more than half. Among them, the power generation from the stepped hydropower plant 2, which is located in the downstream, is the highest among the hydropower plants, with a power contribution of 17.67%. Thermal power plant 1, with its large capacity and relatively low cost, is continuously on during a typical week and contributes 28.23% of electricity generation. Photovoltaic (PV) and wind farms have power contributions of 0.82% and 10.89%, respectively.

Table 5: Typical weekly power consumption contribution

Power supply	Battery power /MW·h	Contribution ratio /%	Power supply	Battery power /MW·h	Contribution ratio /%
Cascade hydropower station 1	13964.42	12.40	Thermal power station 1	31785.93	28.23
Cascade hydropower station 2	19891.65	17.67	Thermal power station 2	8529.61	7.58
Adjustable hydropower station 3	14642.36	13.01	Thermal power station 3	836.45	0.74
Run-of-River hydropower station 4	9751.48	8.66	Photovoltaic power station	12263.52	10.89
Wind farm	927.84	0.82			

Calculation Example 2 examines how uncertainty in wind-generation output affects electricity balance, and wind and photovoltaic unit forecasts are made with an error of 15%. It generates 3,000 scenarios based on Latin hypercube sampling. After reducing the wind-generation scenario, five typical week output curves are achieved as shown in Fig. 4, where panels (a) and (b) represent wind and photovoltaic generation respectively. Each case probability and the power contribution of these resources in different conditions are presented in Table 6. In Fig. 4 there are lower fluctuations in the output of renewables and a lower contribution in a week.

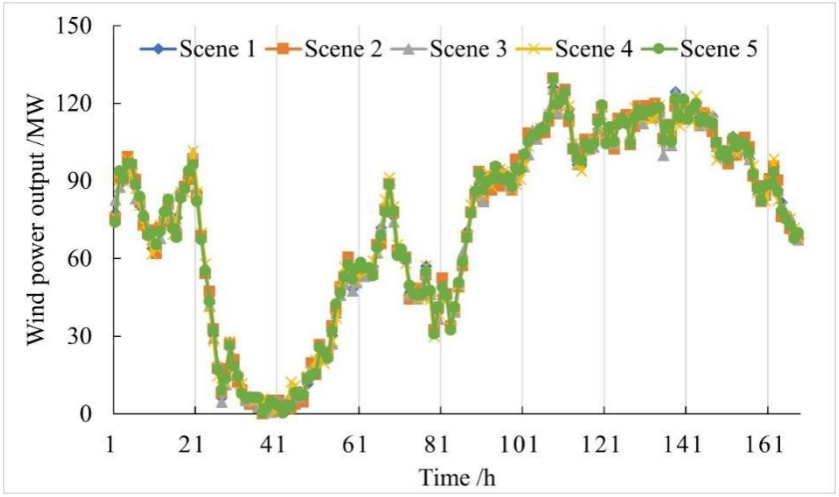

(a) Wind farm

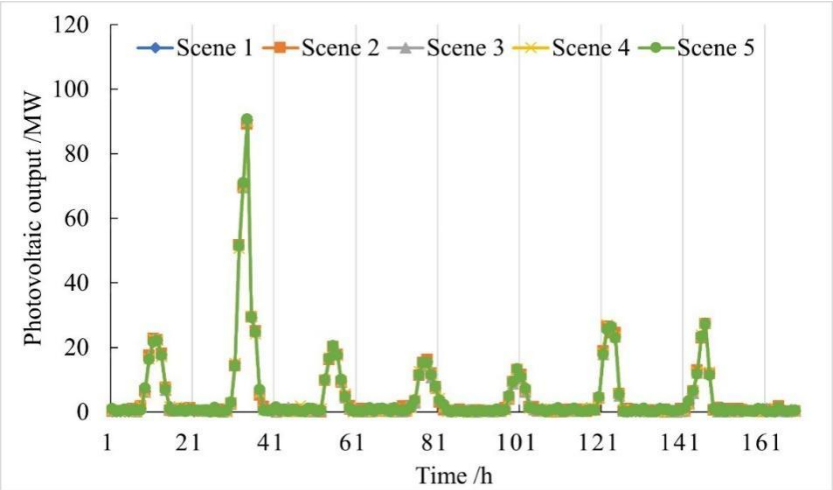

(b) Photovoltaic power station

Figure 4: Output curves of of wind farms and photovoltaic power stations of example 2

Table 6: Contribution of wind and solar power in different scenarios of example 2

Scene	Scene probability	Electricity contribution from wind farms /MW·h	Power contribution of photovoltaic power stations /MW·h
1	0.289	12230.67	820.74
2	0.127	12249.43	824.93
3	0.122	12338.41	819.45
4	0.258	12429.75	820.06
5	0.204	12374.26	827.62

The prediction errors for wind farms and PV plants are further increased in Example 3, and the five scenarios of wind and solar output obtained are shown in Fig. 5. It can be seen that the fluctuation interval of the wind and solar output is significantly larger, requiring more peaking capacity from the system.

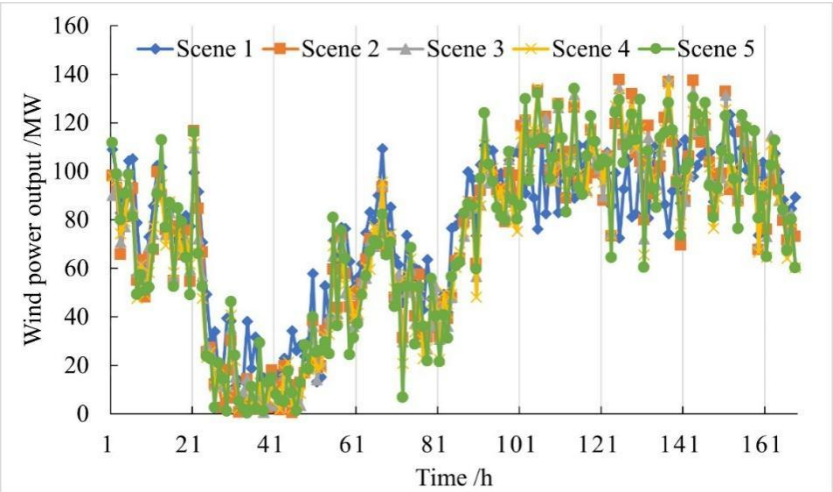

(a) Wind farm

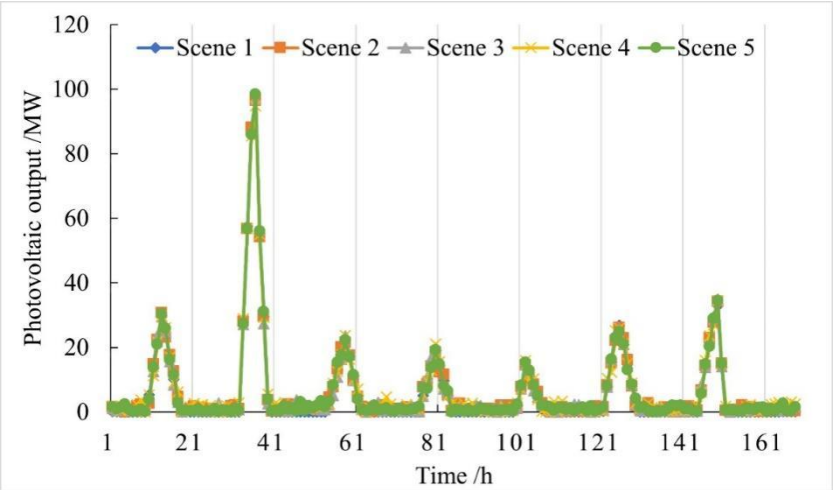

(b) Photovoltaic power station

Figure 5: Output curves of of wind farms and photovoltaic power stations of example 3

The power shares of wind and photovoltaic generation in the different scenarios of Example 3 are reported in Table 7. The comparison of Tables 6 and 7 shows that the difference in the power shares of wind and photovoltaic generation between the scenarios increases as the forecasting error of wind and photovoltaic generation increases.

Table 7: Contribution of wind and solar power in different scenarios of example 3

Scene	Scene probability	Electricity contribution from wind farms /MW·h	Power contribution of photovoltaic power stations /MW·h
1	0.289	12843.24	815.67
2	0.127	12906.12	826.35
3	0.122	13359.63	811.09
4	0.258	13502.75	815.78
5	0.204	13448.19	825.94

A comparison of the operating costs and the number of hours that thermal power plants 1 to 3 are on for a typical week for the three calculation examples is shown in Table 8.

This comparison shows that thermal unit 2 with medium generation costs operates during almost half of the study, while thermal unit 3 with high generation costs acts mostly as a peaking unit and is used only at times when extra peak regulation is needed by the system. On Saturday afternoon, after the inclusion of wind generation uncertainty in Calculation Example 2, thermal unit 3 continues operating for an additional 7 h such that enough spinning reserve is achieved to support the wind power. At other intervals where wind output changes drastically and thermal unit 2 is not available, unit 3 is required to supply the reserve needed by the system. The hydropower station can usually offer sufficient peak shaving capacity to reduce wind power fluctuations during the rest of the time. As the startup time of thermal unit 3 in Example 2 is longer than it is in Example 1, the cost of Example 2, which takes into consideration wind-generation uncertainty, is a little bit higher than that of Example 1. With even greater uncertainty regarding the wind generation in Example 3, the startup hours of thermal units 2 and 3 in Example 3 increase in comparison to Example 2 due to the increased variability of wind generation, leading to the cost of Example 3 reaching 813,859.62 dollars. These findings show that, to have reliable power supply, given the uncertain wind-power output the system will have

to incur additional cost to neutralize the effects of wind-generation fluctuations.

Table 8: The operating costs of typical weeks in example 1 to 3

Calculation example	Cost /yuan	Thermal power station 1 started up /h	Thermal power station 2 started up /h	Thermal power station 3 started up /h
1	796843.21	172	75	27
2	801237.45	172	75	34
3	813859.62	172	79	42

4 Conclusion

The cooperative approach to power balancing renewable energy systems proposed in this paper consists of two parts, namely, an approach to forecasting resources based on space-time using the ARIMA-LSTM framework and a cooperative balancing formulation that is formulated as a multi-objective optimization problem and solved through mixed integer-linear programming.

The MAPE obtained with the ARIMA-LSTM approach presented here is less than both ARIMA (6.05%), LSTM (1.88%) and Elman (9.50%), indicating that it has the closest agreement with the observed values. The ARIMA-LSTM framework remains the most accurate predictor even when the data are increased to one month and one year, and at the same time, it has a running time that is slightly different compared to other models, but more reliable when the training set is small.

The simulation and analytical findings also confirm the validity and utility of the coordinated balancing framework that was put in place to operate the renewable energy systems. The cascade hydroelectric plants have high peaking potential, which is useful in leveling the output of thermal power plants and enhancing the economic performance of the overall power system. As soon as the uncertainty regarding the wind generation output is considered, the extra units are needed to be committed to ensure sufficient load supply. In contrast to the conventional power balance analysis, where wind and photovoltaic generation contribution is represented by one deterministic value, it is now represented by a probabilistic set of power contributions, which does a better job of accounting for the uncertainty related to wind-power output.

Funding

State Grid Chongqing Electric Power Company Economic Research Institute 2025 Research Plan: New Energy Resource Survey and Development Impact Research Service in Chongqing (SGCQJY00XXJS2500035).

References

[1] Usman, M., Ma, Z., Zafar, M. W., Waheed, A., & Li, M. (2021). Analyzing the determinants of clean energy consumption in a sustainability strategy: Evidence from EU-28 countries. Environmental Science and Pollution Research, 28(39), 54551-54564.

[2] Opeyemi, B. M. (2021). Path to sustainable energy consumption: The possibility of substituting renewable energy for non-renewable energy. Energy, 228, 120519.

[3] Liu, J., Wang, Q., Song, Z., & Fang, F. (2021). Bottlenecks and countermeasures of high-

penetration renewable energy development in China. Engineering, 7(11), 1611-1622.

[4] Impram, S., Nese, S. V., & Oral, B. (2020). Challenges of renewable energy penetration on power system flexibility: A survey. Energy strategy reviews, 31, 100539.

[5] Reina, P. (2021). Influence of the Randomness of Renewable Generation in the Multi-Objective Optimization of Electrical Systems. Available at SSRN 3931772.

[6] Haoyu, S., Tianqi, L., Tao, B., Chuan, H. E., Yue, Y. I. N., & Lijie, D. I. N. G. (2020). Operational risk assessment of power system considering wind power and photovoltaic grid connection. Modern Electric Power, 37(4), 358-367.

[7] Habibollahzade, A., Houshfar, E., Ashjaee, M., Behzadi, A., Gholamian, E., & Mehdizadeh, H. (2018). Enhanced power generation through integrated renewable energy plants: Solar chimney and waste-to-energy. Energy conversion and management, 166, 48-63.

[8] Alam, M. S., Al-Ismail, F. S., Salem, A., & Abido, M. A. (2020). High-level penetration of renewable energy sources into grid utility: Challenges and solutions. IEEE access, 8, 190277-190299.

[9] Liu, L., & Xu, J. (2022). Multi-objective generation scheduling towards grid-connected hydro–solar–wind power system based the coordination of economy, management, society, environment: A case study from China. International Journal of Electrical Power & Energy Systems, 142, 108210.

[10] Pierie, F., van Someren, C. E., Kruse, S. N., Laugs, G. A., Benders, R. M., & Moll, H. C. (2021). Local balancing of the electricity grid in a renewable municipality; analyzing the effectiveness and cost of decentralized load balancing looking at multiple combinations of technologies. Energies, 14(16), 4926.

[11] Rosales-Asensio, E., Diez, D. B., & Sarmento, P. (2024). Electricity balancing challenges for markets with high variable renewable generation. Renewable and Sustainable Energy Reviews, 189, 113918.

[12] Kath, C., Nitka, W., Serafin, T., Weron, T., Zaleski, P., & Weron, R. (2020). Balancing generation from renewable energy sources: Profitability of an energy trader. Energies, 13(1), 205.

[13] Yang, M., Wang, D., & Zhang, W. (2024). A novel ultra short-term wind power prediction model based on double model coordination switching mechanism. Energy, 289, 130075.

[14] Zhang, J., Liu, D., Li, Z., Han, X., Liu, H., Dong, C., ... & Xia, Y. (2021). Power prediction of a wind farm cluster based on spatiotemporal correlations. Applied Energy, 302, 117568.

[15] Su, Y., Zhang, M., Cao, L., Chen, Y., & Tian, Y. (2026). Spatio-temporal Graph Neural Network with Fourier features for multi-site photovoltaic power forecasting. Electric Power Systems Research, 251, 112171.

[16] Admasie, S., Song, J. S., & Kim, C. H. (2023). Optimal coordinated generation scheduling considering day-ahead PV and wind power forecast uncertainty. IET

Generation, Transmission & Distribution, 17(11), 2545-2562.

[17] Su, Z., Zheng, G., Hu, M., Kong, L., & Wang, G. (2024). Short-term load forecasting of regional integrated energy system based on spatio-temporal convolutional graph neural network. Electric Power Systems Research, 232, 110427.

[18] Ge, C., Yan, J., Zhang, H., Li, Y., Wang, H., & Liu, Y. (2024). Joint short-term power forecasting of hydro-wind-photovoltaic considering spatiotemporal delay of weather processes. Renewable Energy, 237, 121679.